

ARTICLE OPEN



Resolving few-layer antimonene/graphene heterostructures

Tushar Gupta¹, Kenan Elibol², Stefan Hummel^{2,3}, Michael Stöger-Pollach⁴, Clemens Mangler², Gerlinde Habler⁵, Jannik C. Meyer², Dominik Eder¹✉ and Bernhard C. Bayer^{1,2}✉

Two-dimensional (2D) antimony (Sb, “antimonene”) is of interest in electronics and batteries. Sb however exhibits a large allotropic structural diversity, which is also influenced by its support. Thus, Sb heterostructure formation is key in 2D Sb integration. Particularly, 2D Sb/graphene interfaces are important. We thus study here few-layered 2D Sb/graphene heterostructures with atomic resolution (scanning) transmission electron microscopy. We find two Sb morphologies to coexist: first, a 2D morphology of layered β -Sb with β -Sb(001)||graphene(001) texture. Second, one-dimensional Sb nanowires which can be matched to β -Sb[2-21] \perp graphene(001) and are closely related to cubic Sb(001)||graphene(001). Importantly, both Sb morphologies show rotational van-der-Waals epitaxy with graphene. Both are resilient against oxidation, although superficial Sb-oxide formation merits consideration, including epitaxial Sb₂O₃(111)/ β -Sb(001) heterostructures. Exact Sb growth behavior depends on processing and substrate properties including, notably, the support underneath the graphene. Our work elucidates the rich phase and epitaxy landscape in 2D Sb and 2D Sb/graphene heterostructures.

npj 2D Materials and Applications (2021)5:53; <https://doi.org/10.1038/s41699-021-00230-3>

INTRODUCTION

Among the two-dimensional (2D) pnictogens (i.e., group 15/VA elements, including P, As, Sb, and Bi)^{1–4} particularly mono- and few-layered 2D Sb (“antimonene”) has recently attracted increasing research interest^{5,6}. Firstly, this is due to 2D Sb’s peculiar electronic properties toward novel 2D electronics including layer-dependent (semi-)metal-to-semiconductor transition^{7,8} high carrier mobilities⁹, strain-tunable indirect-to-direct band gap transition^{7,8}, and the possibility of 2D and 3D topological insulator behavior for mono-¹⁰ and few-layered⁵ 2D Sb, respectively. Secondly, the recent high interest equally results from 2D Sb’s high suitability for sustainable energy and catalysis applications, including as an anode material in next-generation Li- and Na-ion batteries^{11–21} as well as for (electro)catalysis^{22–24}, supercapacitors²⁵, charge extraction in photovoltaics²⁶, and thermoelectrics²⁷.

Sb however shows a large allotropic/polymorphic structural diversity. This includes several layered, potential 2D forms^{8,28–31} such as in particular the thermodynamically most stable, rhombohedral, buckled honeycomb-structured β -Sb (A7, R-3m, 166)^{22,23,30–44} and the metastable orthorhombic, puckered “washboard”-structured α -Sb (A17, cmca, 64)^{31,45,46}. In addition, several nonlayered metastable allotropes at high pressure and in thin film form have been reported including simple cubic, body-centered-cubic, face-centered-cubic, and hexagonally close-packed Sb^{47–56}. Most of these phases are related via small atomic rearrangements^{31,54–56}, and some even have been suggested to show thickness-dependent phase transitions in nanostructures³¹. This polymorphicity calls for close control over Sb’s structure in any potential synthesis scenario for the various desired application fields. The structure of Sb deposits is however not only determined by kinetic growth process conditions but is also intimately linked to the Sb deposits’ support, an effect which is exacerbated for ultrathin 2D Sb. Therefore, understanding Sb heterostructure formation is key for controllable 2D Sb growth. This is true not only for Sb’s use in 2D electronics, where typically

laterally large, defect-free 2D Sb films are desired³³, but also for Sb’s use in catalysis and energy applications, where often nanosized 2D Sb deposits with a large number of edges are preferred^{22,23}.

Among the various possible Sb heterostructures⁵, in particular, 2D Sb/graphene interfaces are of prime importance for two reasons: first, in the context of catalysis and energy applications, Sb/carbon hybrids are emerging as a highly useful materials combination, e.g., in batteries^{11–20}, electrocatalysis^{22,23}, and supercapacitors²⁵. 2D Sb/graphene heterostructures can readily approximate such Sb/carbon hybrids in order to understand their as-of-yet little elucidated interface properties. Second, in the context of 2D electronics, recent work has suggested that device contacts formed by 2D Sb/graphene heterostructures could be technologically advantageous toward tuning contact resistances^{57,58}.

The structural properties and formation mechanisms of Sb heterostructures including 2D Sb/graphene, remain however as-of-yet largely underexplored, in particular at the atomically resolved level. To address this, we provide here an atomic-scale (scanning) transmission electron microscopy ((S)TEM) investigation into the properties of a few-layered 2D Sb/graphene heterostructure model system that, as we find, readily emulates Sb/carbon heterostructures as manufactured by vapor phase techniques for electronics^{38,48,50,51} and also as synthesized by wet-chemistry routes for energy applications^{12,14,15,19,20}. Our approach thereby facilitates direct assessment of interfacing and epitaxial effects in 2D Sb/carbon heterostructures, with graphene also acting as an ideal support⁵⁹ for the employed atomic resolution (S)TEM techniques⁶⁰.

Our work reveals in our 2D Sb/graphene heterostructures the coexistence of a 2D growth morphology of layered β -Sb(001)||graphene(001) phase and texture as well as of a one-dimensional (1D) Sb growth morphology. The latter 1D morphology can be matched not only to β -Sb with β -Sb[2-21] \perp graphene(001) texture but also to a nonlayered, thermodynamically nonpreferred cubic

¹Institute of Materials Chemistry, Vienna University of Technology (TU Wien), Vienna, Austria. ²Faculty of Physics, University of Vienna, Vienna, Austria. ³GETec Microscopy GmbH, Vienna, Austria. ⁴USTEM, Vienna University of Technology (TU Wien), Vienna, Austria. ⁵Department of Lithospheric Research, University of Vienna, Vienna, Austria. ✉email: dominik.eder@tuwien.ac.at; bernhard.bayer-skoff@tuwien.ac.at

Sb(001)||graphene(001). Importantly, both Sb morphologies show preferred relative crystallographic (mis)orientations with respect to the supporting graphene monolayer lattice, indicating that rotational van-der-Waals (vdW) epitaxy can readily exist in 2D Sb/graphene heterostructures. Both Sb morphologies are found to be well resilient against environmental oxidation in ambient atmosphere although superficial surface oxidation is shown to be important to consider, particularly due to here suggested formation of epitaxial Sb₂O₃(111)/β-Sb(001) heterostructures as top layer. We find that exact Sb growth results are sensitive on employed processing techniques and substrate properties including, notably, the nature of the support underneath the direct graphene support. Our work thereby provides fundamental insights into the rich phase and epitaxy relations in 2D Sb and 2D Sb/graphene heterostructures.

RESULTS AND DISCUSSION

Morphology and structure

We first characterize in Fig. 1 the morphology and structure of the few-layer Sb on graphene model system, which is prepared by physical vapor deposition (PVD) of Sb onto chemical vapor deposited (CVD) monolayer graphene. We first focus on optimized Sb deposition conditions toward high Sb crystallinity, with the wider parameter space of the Sb PVD on graphene being discussed further below. The nominal 10 nm thick Sb deposits in Figs. 1–4 were thermally evaporated onto monolayered CVD graphene films^{61,62}. During Sb PVD (base pressure ~10⁻⁵ mbar), the graphene substrates were held at room temperature (RT) and also at controlled temperatures of 150 and 250 °C. The graphene either remained on its Cu CVD catalyst foils^{61,62} during Sb PVD (Figs. 1a, b and 2) or was additionally also transferred prior to Sb PVD to be suspended as a freestanding monolayer membrane across holey TEM grids⁶³ (i.e., no Cu foils underneath, Figs. 1c–g, 3, and 4). Nominal deposited Sb thickness was measured via a coexposed (nonheated) quartz crystal microbalance (QMB). After Sb deposition, samples were stored in ambient air.

The scanning electron microscopy (SEM) image of the 250 °C deposition in Fig. 1a reveals that under our optimized PVD conditions, the Sb deposits on the graphene form isolated islands with two distinctly different base shapes: first are flat 2D Sb deposits with (truncated) hexagonal or (truncated) triangular base shapes. Second are rod-like 1D Sb deposits with rectangular bases. Lateral extents of all Sb deposits are in the range of tens to hundreds of nm. While such lateral sizes are small for device fabrication in 2D electronics, they are well compatible with the requirements for 2D Sb catalysis and energy applications²². Importantly, such feature sizes also provide a convenient Sb/graphene heterostructure model system for elucidation of Sb phases and interfacing by high-resolution (S)TEM. Notably, as shown in Fig. 1a, the edges of both the triangular-/hexagonal-shaped and the rod-shaped Sb deposits show a high degree of visually apparent directional alignment amongst each phase type, respectively. This is a first indication of potential epitaxy effects between the Sb deposits and their graphene support and will be further examined below.

The Raman spectrum corresponding to the 250 °C deposition in Fig. 1b displays primarily two peaks at low wavenumbers that are characteristic for elemental Sb (117 cm⁻¹; 154 cm⁻¹). These peaks are best matched with E_g and A_{1g} modes of few-layer β-Sb, respectively, but are also potentially consistent with α-Sb and/or pressure-induced phases of Sb^{8,31,33,46,54}. We note that thicker Sb deposits may be overrepresented in Raman intensity^{42,43}. Significant volume Sb-oxide formation can be excluded based on our Raman data as the signal intensity at wavenumbers corresponding to Sb oxides is comparatively weak (e.g., for thermodynamically most stable Sb₂O₃ expected at ~190 and

250 cm⁻¹)⁶⁴. The minor peak at ~215 cm⁻¹ is related to minor Cu-oxide formation on bare regions of the Cu support during ambient air storage^{65,66}. Raman peaks characteristic for graphene (G at 1593 cm⁻¹ and 2D at 2701 cm⁻¹) are also found in Fig. 1b, consistent with the high quality CVD graphene used as substrate^{61,62}. The absence of a significant defect-related D peak at ~1350 cm⁻¹ confirms that the CVD graphene support was not degraded during Sb PVD. Thereby our Raman data also confirm that no covalent Sb–carbon bond formation has occurred and that our 2D Sb/graphene interfaces are of vdW type³⁸, consistent with theoretical predictions^{8,57,58}.

To assess the crystallographic structure of the Sb deposits in a localized fashion, we employ in Fig. 1c–g aberration-corrected, atomically resolved and element-specific STEM (Nion UltraSTEM 100 at 60 kV electron acceleration voltage) in annular dark field (ADF)⁶⁰ mode to image individual Sb deposits at high resolution in top plan view. Corresponding ADF STEM and bright-field (BF) TEM data from focused ion beam (FIB) cross sections in Fig. 2 provide a complementary side view of the Sb deposits. Supplementary Figs. 2 and 3 provide atomic models and Fourier transform (FT)/selected area electron diffraction (SAED) simulations of all identified phases. We note that under our STEM imaging conditions no electron beam induced phase transitions or materials modifications to the Sb deposits were observed^{67–69}.

The first group of interest is the flat Sb deposits from Fig. 1a with (truncated) hexagonal (Fig. 1c) or triangular base shape (Fig. 1d). The phase identification for these structures is straightforward: at atomic resolution and view from top, all flat hexagonal/triangular deposits show a sixfold symmetric appearance that can be best indexed via the FT of their atomic resolution images to rhombohedral β-Sb viewed along the [001] zone axis (Fig. 1h), i.e., with the basal (001) layers of the layered 2D β-Sb parallel to the graphene(001) substrate (i.e., β-Sb[001]⊥graphene(001) = β-Sb(001)||graphene(001)). This phase identification to β-Sb(001) is also fully corroborated by the corresponding side view of a triangular/hexagonal deposits in Fig. 2b–d, which clearly resolves the layered nature of the β-Sb(001) when viewed along the [110] zone axis, with the β-Sb(001) planes parallel to the graphene(001) substrate. Delineating projected edge directions correspond to [100], [010], and [110] in the top view STEM images for both hexagonal and triangular β-Sb (Fig. 1c, d). Hexagonal and triangular deposits typically appear flat in STEM images, indicating (001) top surfaces. The observation of 2D β-Sb(001)||graphene(001) is in line with recent literature^{31–39}.

The second group of interest is the rod-like 1D Sb deposits with rectangular bases (Fig. 1e–g). In top view at atomic resolution, these structures always show a FT with fourfold symmetry. Their phase identification is less straightforward: on the one hand, the STEM data agree with β-Sb when viewed along the [2-21] zone axis, i.e., at a texture of β-Sb[2-21]⊥graphene(001). Notably, β-Sb with [2-21] zone axis perpendicular to support does not have a defined low (hkl) value interface plane parallel to the support when viewed from the side, but only slightly inclined base planes (Fig. 1i; an approximation for an interface plane would be β-Sb(10 -10 23)). β-Sb[2-21] is closely related to AA-stacked α-Sb multilayers via a small shear deformation³¹. Recently, a thickness-dependent crossover from α-Sb to β-Sb[2-21] has been suggested to occur in 1D Sb deposits³¹. On the other hand, the fourfold symmetry STEM images of the 1D rod-like Sb deposits also matches well with a thermodynamically nonpreferred simple cubic, nonlayered Sb polymorph viewed along its [001] zone axis (Fig. 1j), i.e., cubic Sb [001]⊥graphene(001) = cubic Sb(001)||graphene(001)^{47,50}. Cubic Sb polymorphs are related to rhombohedral β-Sb via a unidirectional deformation^{54–56}. While the existence of cubic Sb in bulk form has been a long-standing matter of debate in the literature^{52–56}, cubic Sb is typically associated with high pressure conditions but has also been reported to occur in Sb thin films, presumably formed via substrate-induced stress^{47–56}. Notably, structurally β-Sb

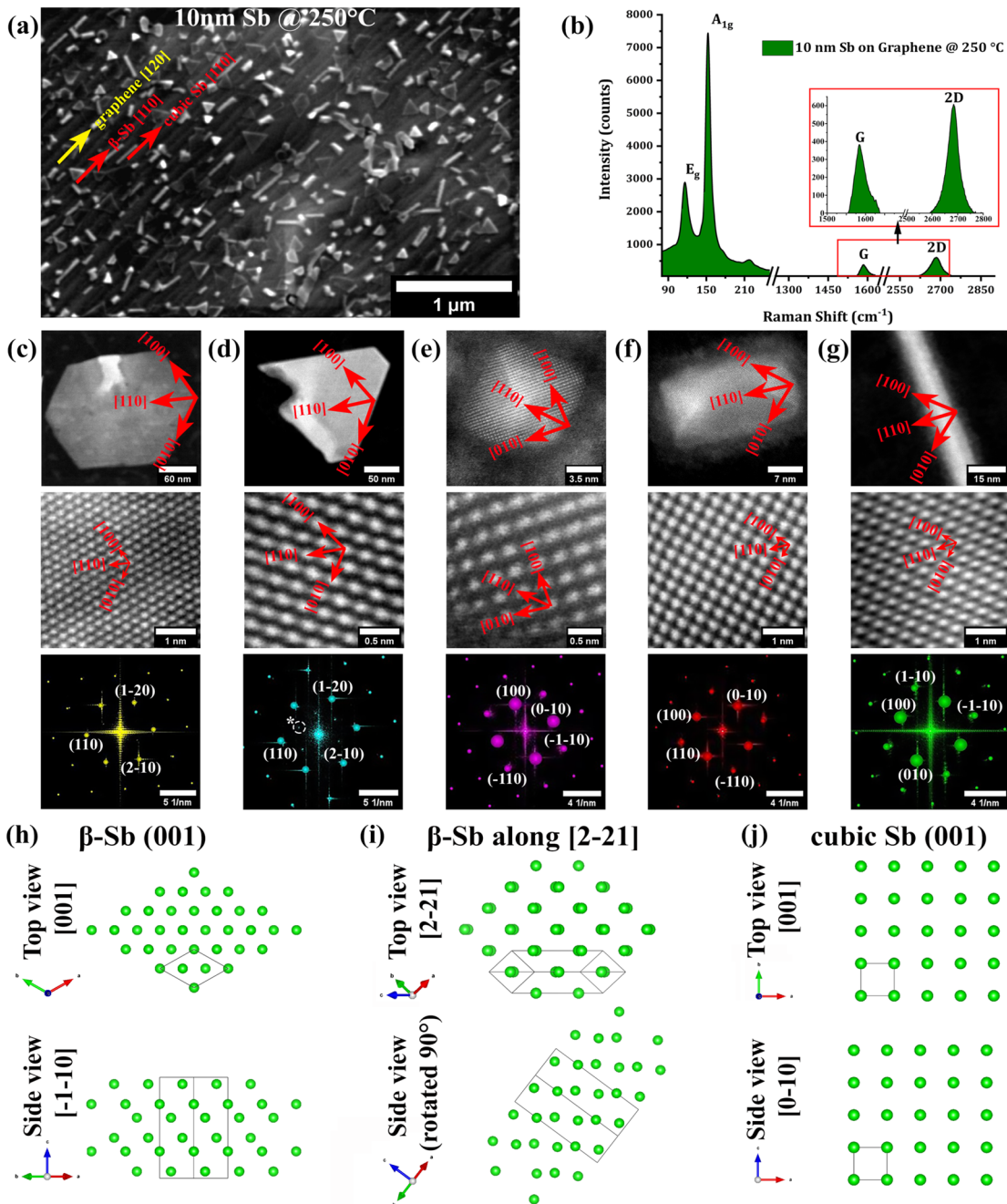


Fig. 1 Morphology and structure. **a** SEM image and **b** Raman spectrum of 10 nm Sb deposited at 250 °C onto Cu-supported CVD graphene. Salient lattice directions in the graphene and the Sb are labeled in **a**, as identified in the main text. **c–g** ADF STEM images of individual particles of 10 nm Sb deposited at 150 and 250 °C onto suspended monolayer graphene, showing overview (top) and atomic resolution images (middle) and corresponding FTs (bottom). The FTs are indexed to β -Sb(001) viewed along [001] zone axis (**c**, **d**) and cubic Sb(001) viewed along [001] zone axis (**e–g**), respectively. Corresponding salient crystallographic directions are superimposed over the ADF images. The sixfold symmetric “*”-indexed reflection set in **d** is ascribed cubic Sb_2O_3 viewed along the [111] zone axis and corresponds to Sb_2O_3 (2-20) reflection family, as described below. False-color coded ADF STEM images of overview and atomic resolution images can be found in Supplementary Fig. 1. **h–j** Atomic models of β -Sb(001), β -Sb[2-21], and cubic Sb(001), respectively. For further information on atomic models and FT simulations see Supplementary Figs. 2 and 3.

[2-21] (and AA α -Sb multilayers) and cubic Sb(001) structures are all closely related and may gradually transition into each other^{31,54–56}. This makes their differentiation difficult and partly ambiguous. This is also underlined by, e.g., the cross-sectional TEM of a rod-like Sb deposit in Fig. 2d which shows lattice planes with a principal spacing of ~ 0.3 nm. These are consistent with β -Sb[2-21] as well as cubic Sb(001) viewed from the side (Fig. 1i, j). Therefore, for the remainder of this report, we refer to the 1D Sb morphology

as “ β -Sb[2-21]/cubic Sb(001)” phase and texture, suggesting that the 1D rods are compatible with both β -Sb[2-21] \perp graphene(001) and cubic Sb(001) \parallel graphene(001). For determination of β -Sb[2-21]/cubic Sb(001) in-plane epitaxial relations to graphene support, delineating projected edge directions and similar discussion below we will predominantly use the cubic Sb unit cell and associated (hkl) plane and [uvw] direction notation since this conveniently simplifies the description of the crystallographic

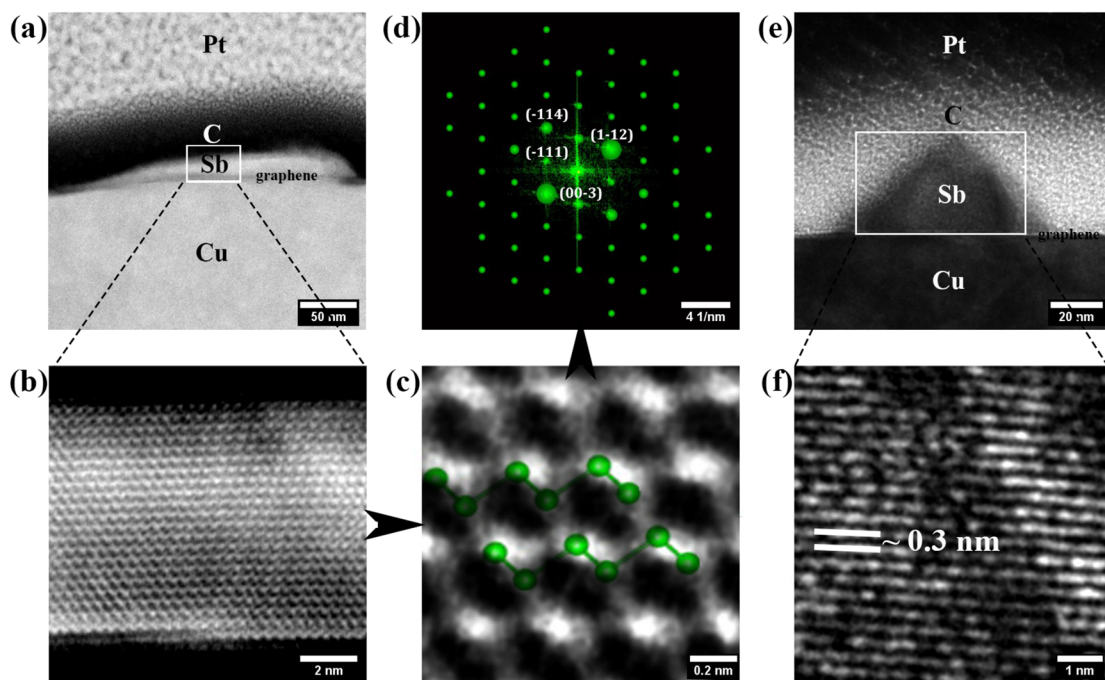


Fig. 2 Cross-sectional STEM/TEM of 10 nm Sb deposited onto Cu-supported graphene. ADF STEM of a β -Sb(001) deposit in overview (a), intermediate (b), and high resolution (c). **d** The FT of **c** indexed to β -Sb(001) viewed along the [110] zone axis. In **c**, a schematic of the β -Sb(001) layers is superimposed as illustration. BF-TEM of a β -Sb[2-21]/cubic Sb(001) deposit in overview (e) and at high resolution (f).

system compared to the inclined plane β -Sb[2-21] description. Delineating projected edge directions in the top view STEM images are cubic Sb [110] for the rods (Fig. 1e–g). Consequently, the rods long axis is cubic Sb [110] direction. Figures 1e–g and 2e show that the 1D morphology does not have a flat top surface but rather very strong faceting to a pyramidal shape over a square (Fig. 1e) or rectangular (Fig. 1f, g) base. To best reproduce the observed angles in Figs. 1e–g and 2e, the delineating faceted surfaces have to be of (223) family in cubic Sb notation (Supplementary Fig. 4). Alternatively, also (111) family facets can provide a reasonable match. 1D Sb morphologies with fourfold atomic symmetries that coexist with 2D β -Sb(001) have been observed in older work on Sb/graphite^{50,51} and also recent work on Sb/graphene³¹, albeit other recent work under very similar conditions for Sb/graphene heterostructures did not observe 1D nanostructure growth³⁸. We note that one recent paper⁷⁰ ascribed 1D Sb nanostructures to β -Sb(001), albeit without providing direct crystalline structure confirmation for their assignment.

We have confirmed the morphology-structure relation of triangular/hexagonal base shape corresponding to layered 2D β -Sb(001) and rectangular rod base shape corresponding to β -Sb[2-21]/cubic Sb(001) via >60 atomic resolution STEM, lattice resolution TEM, and SAED observations. This makes us confident that we can safely assign the crystallographic phase of a deposit via its macroscopic base shape as observed in lower magnification SEM or atomic force microscopy (AFM) data⁵¹.

Following this approach, AFM data (taken via conventional AFM as well as via correlated AFM-SEM, GETec AFSEM⁷¹, see Supplementary Fig. 5) indicate for depositions at 250 °C, for the layered 2D β -Sb(001) deposits, a minimum thickness of 4.7 nm (equivalent to ~12 layers^{8,29,42}, i.e., few-layer antimonene), and an average thickness (\pm standard deviation) of 21 ± 14 nm. The 1D rod-like β -Sb[2-21]/cubic Sb(001) deposits are relatively thicker, with a minimum thickness of 10 nm and an average thickness of 31 ± 10 nm. To estimate the relative abundance of 2D β -Sb(001) and 1D β -Sb[2-21]/cubic Sb(001) in our deposits, we compute from SEM and AFM images for the 250 °C depositions, both

domain number counts and average equivalent feature sizes (see “Methods” section for calculation) for each phase: via this analysis, we find a lower number fraction of 2D β -Sb(001) domains (40 ± 1 count-%) compared to β -Sb[2-21]/cubic Sb(001) (60 ± 1 count-%). These 2D β -Sb(001) domains grow to however cover a relatively larger area (60 ± 5 area-% for 2D β -Sb(001) vs. 40 ± 5 area-% for β -Sb[2-21]/cubic Sb(001)). The observation that the 2D β -Sb(001) islands grow to larger lateral sizes is also reflected in a larger maximum and average equivalent feature size for the 2D β -Sb(001) (maximum: 260 nm; average: 113 ± 95 nm) compared to the β -Sb[2-21]/cubic Sb(001) (maximum: 130 nm; average: 72 ± 54 nm).

Comparing our results with the prior literature, we note that overall morphology and size of our Sb domains on carbon substrates are consistent not only with vacuum-based vapor deposition techniques as usually used in electronics^{38,48,50,51} (akin to our PVD synthesis) but also with several wet-chemistry synthesis routes (including using SbCl_3 ^{12,14,19,20} and ball-milled and annealed Sb/carbon mixtures¹⁵) as usually used in energy materials synthesis. This highlights that our here investigated 2D Sb/graphene heterostructure model system is relevant to a wide range of synthesis conditions in electronics and energy-related applications of Sb on carbon.

In terms of application potential, we note that trigonally deformed Sb (like simple cubic Sb) has recently been predicted to feature superior thermoelectrical performance over β -Sb⁵⁶. Given that monolayered 2D β -Sb has been predicted to surpass all other pristine 2D materials in terms of thermoelectric performance²⁷, future studies on band structure and electronic properties of the here observed β -Sb[2-21]/cubic Sb(001) deposits merit consideration.

vdW epitaxy

So far our data have shown that we have grown 2D Sb/graphene heterostructures, where the Sb deposits are comprised of two coexisting morphologies, namely few-layer 2D β -Sb(001) and 1D nanorods β -Sb[2-21]/cubic Sb(001). Importantly, for both these Sb morphologies Fig. 1a indicated a high degree of directional

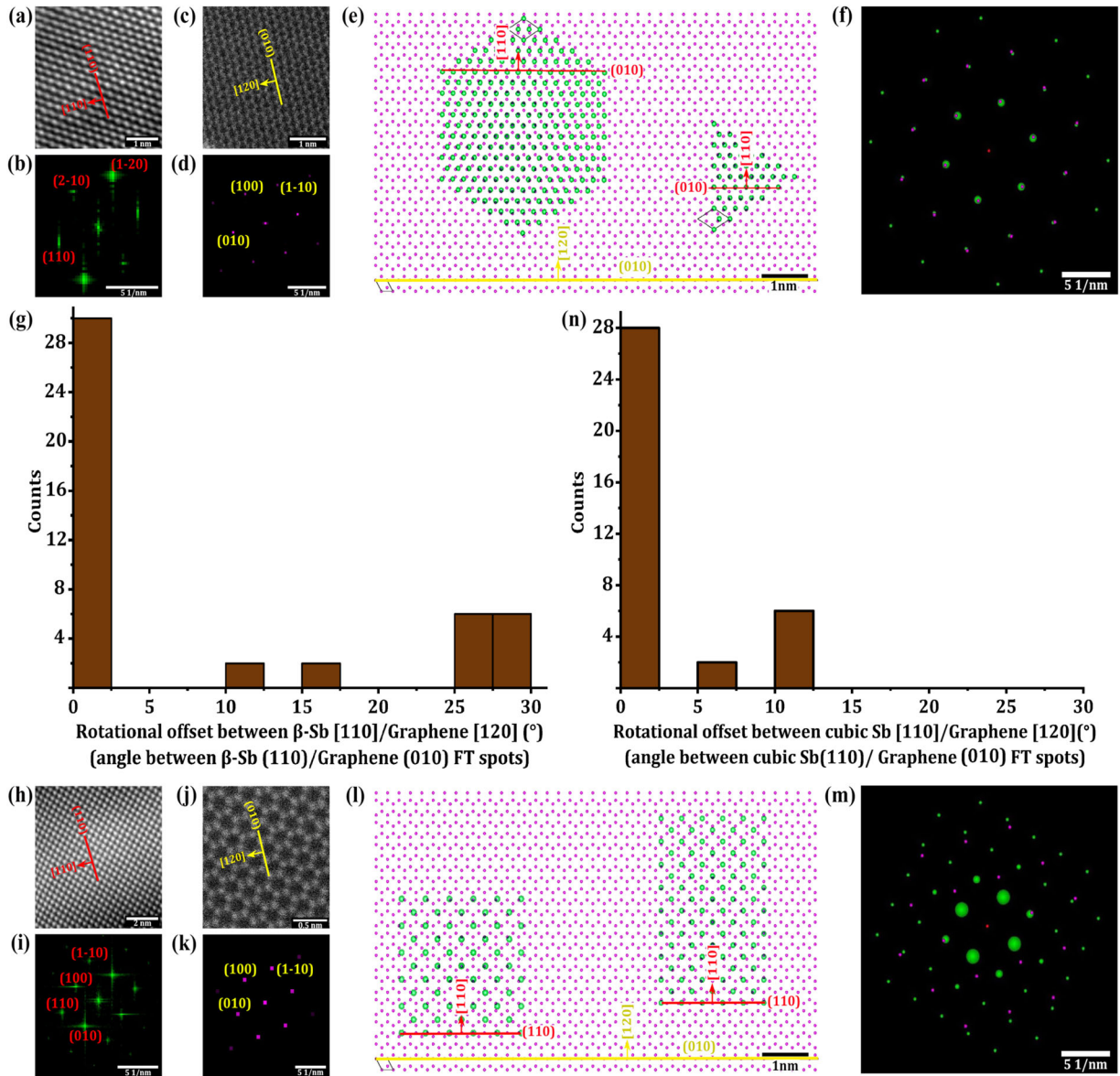


Fig. 3 Epitaxy. **a** Atomic resolution ADF STEM and **b** corresponding FT of a β -Sb(001) particle on suspended graphene. **c** ADF STEM and **d** FT of the graphene(001) lattice just adjacent to the particle in **a**. The FTs are indexed to their corresponding phases and in the ADF images salient planes and directions are highlighted. **e** Atomic models showing in-plane vdW epitaxial relations derived from the data in **a–d**, suggesting β -Sb(001)||graphene(001)/ β -Sb[110]||graphene[120], i.e., angle between β -Sb[110] and graphene[120] = 0° . **f** The overlay of simulated FTs corresponding to the models in **e**. **g** Histogram of multiple measurements similar to **a–f** showing a distribution of (mis)rotation angles between β -Sb[110] and graphene[120] which peaks at 0° , confirming the suggested in-plane vdW epitaxy relation depicted in **e** to be preferred. **h–n** Corresponding measurements for cubic(001) deposits on suspended graphene, yielding a preferred cubic Sb(001)||graphene(001)/cubic Sb[110]||graphene[120] in-plane vdW epitaxy relation. For epitaxial relations in β -Sb[2-21] notation see Supplementary Fig. 7. Note that direction vector lengths in **a, c, e, h, j, and l** are not to scale but enlarged for readability.

alignment of their respective domain edges on the monolayer graphene support. Given the vdW nature of the Sb/graphene interface (Fig. 1b), three mechanisms could contribute to such alignment: first is direct rotational vdW epitaxy between the growing Sb and its graphene support directly underneath⁷². For 2D β -Sb(001) direct epitaxial relationships with various substrates have been reported, including WSe₂³⁹, tellurides^{32,36}, mica³³, and Ge³⁵. Particularly, for β -Sb(001) on graphene prior work has given a mixed picture: Some work³⁸ reported rotational vdW epitaxy for β -Sb/graphene via indirect measurements, while other work observed no such epitaxy^{31,44,50,51}. For the 1D nanorod β -Sb[2-21]/cubic Sb(001), epitaxial effects have to date not been

reported^{31,51}. Therefore, the question if direct vdW epitaxy is prevalent in the Sb/graphene system remains open. Second, however, complicating elucidation of this question also recently reported remote epitaxy needs consideration in which epitaxy is impressed remotely between a deposit and its underlying substrate through an intermediate 2D layer⁷³. In the present work, this would involve interactions between Sb and the underlying Cu foils impressed through the graphene monolayer³⁸. Notably, in this scenario, the graphene could also be required to act as a diffusion barrier to prevent chemical reactions between Sb and Cu^{74,75}, thus actually actively facilitating the remote epitaxy. Third, in contrast to the atomic-scale epitaxy, the third possibility

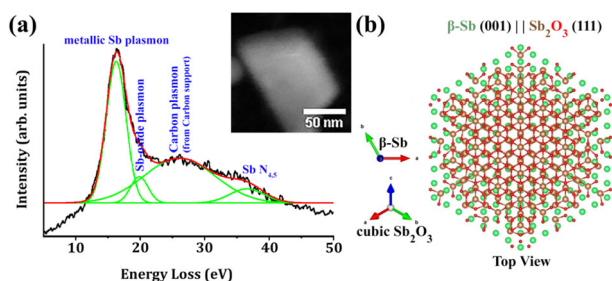


Fig. 4 Oxidation. **a** VEELS spectrum of the β -Sb(001) crystal on suspended graphene (on amorphous carbon support) in the ADF STEM in the inset. The spectrum was acquired after ~ 8 months ambient air exposure of the sample. The VEELS data are fitted to the components labeled and described in the main text. Measurements on multiple β -Sb(001) and β -Sb[2-21]/cubic Sb(001) deposits showed similar results in terms of only low Sb-oxide plasmon signal. Note that the metallic Sb plasmon has the same energy for β -Sb(001) and β -Sb[2-21]/cubic Sb(001) in our VEELS measurements⁹⁶. **b** Atomic model of the suggested $\text{Sb}_2\text{O}_3(111)||\beta\text{-Sb}(001)$ heterostructure that forms from ambient air exposure on β -Sb(001) crystals.

involves macroscopic corrugations on the support (e.g., Cu surface steps) that result in alignment via preferred heterogeneous nucleation sites (e.g., at steps) and diffusion directing effects⁷⁶.

From SEM data as in Fig. 1a alone, these three possible causes of the observed Sb alignments are hard to disentangle: first, direct vdW epitaxy would be readily compatible with the observed lateral length scales of alignment in Fig. 1a as the lateral size of our CVD graphene domains is in the tens of μm range^{61,62,67}. Therefore, the field of view in Fig. 1a represents most likely only one single-crystalline graphene domain (although not confirmable by SEM) which could facilitate rotational alignment over the entire field of view. Second, however, graphene-mediated remote epitaxy between Sb and Cu is also conceivable for Fig. 1a, since the Cu grain sizes in our Cu foils after graphene CVD are in the mm-range^{61,62}. Notably, no Cu grain boundary is visible in Fig. 1a⁶², thus confirming a single Cu orientation across the field of view in Fig. 1a. However, as we show in Supplementary Fig. 6, direct deposition of Sb on Cu (i.e., without graphene in between) does not show any indications of epitaxial order in the Sb deposits under our conditions⁷⁴. Nevertheless, a graphene-mediated remote epitaxy mechanism between Sb and Cu³⁸ cannot be excluded based on Fig. 1a. The third possibility, i.e., surface corrugations on the Cu support, could also direct the Sb deposits, although not resolvable in Fig. 1a.

To disentangle these three possible influences, we investigate in Fig. 3 the relative orientation of Sb depositions at 150 and 250 °C directly onto suspended monolayer graphene membranes, i.e., without Cu foil underneath. In doing so, we exclude any possible indirect influence of Cu underneath the graphene on the Sb alignment (i.e., we exclude remote epitaxy and an influence from Cu surface corrugations). In particular, we correlate the STEM-derived orientation (via FT analysis) of the lattice of the Sb deposits with the underlying graphene lattice orientation measured adjacent to the Sb deposit within a few nm distance⁶⁷ for multiple Sb deposits of both morphologies (β -Sb(001): Fig. 3a–g; cubic Sb(001): Fig. 3i–n; β -Sb[2-21]: Supplementary Fig. 7). Via plotting histograms of the relative rotational (mis)orientations of the graphene [120] direction (armchair direction) and prominent orientations in the two respective Sb lattices (β -Sb [110]: Fig. 3g; cubic Sb [110]: Fig. 3n; β -Sb[2-21]: Supplementary Fig. 7), we find clear peaks in the (mis)orientation distributions for both Sb phases. This unambiguously suggests direct epitaxy effects to be present between the graphene and *both* Sb phases. In particular 2D β -Sb shows a preferred misorientation of $\sim 0^\circ$ between the graphene [120] and the β -Sb [110] in-plane directions (i.e., β -Sb [110]||graphene[120]), as shown in the model

in Fig. 3e. In addition, a secondary, less prominently preferred misorientation appears at an offset of $\sim 30^\circ$ for β -Sb [110] and graphene [120] in Fig. 3e. For cubic Sb, we find a single preferred misorientation of $\sim 0^\circ$ between the graphene [120] and cubic Sb [110] directions (i.e., cubic Sb[110]||graphene[120]), as depicted in the model in Fig. 3l. Notably, since the long axis direction of the cubic Sb rods is [110] (Fig. 1), this implies that the rods' long axes are aligned along the graphene [120] direction. Notably, this preferential alignment may be intertwined with symmetry breaking of the cubic Sb(001) toward anisotropic rod formation.

To cross-check these STEM-derived rotational vdW epitaxy relations via the SEM data in Fig. 1a, we label the salient directions by colored arrows in Fig. 1a: we first assign the long axis of the cubic Sb rods to cubic Sb [110] based on Fig. 1e–g (red arrow). Based on cubic Sb[110]||graphene[120], this direction then coincides with graphene [120] direction (yellow arrow). Thereby it becomes apparent that for most of the β -Sb triangles in Fig. 1a one triangle edge (red arrow) coincides with the graphene[120] direction. This is exactly as expected from the β -Sb [110]||graphene[120] relation and from the observation that one edge direction of the triangles is typically β -Sb [110], as inferred in Fig. 1c, d. Consequently, STEM and SEM data consistently suggest direct Sb/graphene vdW epitaxy for both β -Sb and cubic Sb with the preferred overall relations β -Sb(001)||graphene(001)/ β -Sb [110]||graphene[120] and cubic Sb(001)||graphene(001)/cubic Sb[110]||graphene[120], respectively. (For epitaxial relations in β -Sb[2-21] notation see Supplementary Fig. 7).

Prior work has investigated possible epitaxy between Sb polymorphs and graphene (and graphite) with mixed results: early work did not find evidence for epitaxy in β -Sb/graphite (but had only limited statistics measured)⁵¹. Also, recent other studies did not observe epitaxy in β -Sb/graphene^{31,44}. In contrast, another recent study of β -Sb and Cu-supported graphene suggested epitaxy for β -Sb/graphene to exist based on indirect measurements, identifying two preferred orientations of (in our notation) 0° and 30° offset between β -Sb [110] and graphene [120]³⁸. This is in good agreement with our findings in Fig. 3g which are based on direct observations of the β -Sb/graphene interface. For β -Sb[2-21]/cubic Sb(001) on graphite no evidence for epitaxy has been reported prior^{31,51}. In contrast, we here find strong evidence also for rotational vdW epitaxy in the β -Sb[2-21]/cubic Sb(001)/graphene system. Combined, our observations show that vdW epitaxy can be enforced on 2D and 1D Sb deposits on graphene.

Oxidation susceptibility

After having identified the nature of our Sb deposits and their relation to the graphene support, we turn to the oxidation susceptibility of our Sb deposits. Oxidation susceptibility is of significant importance in terms of processing and applications. In addition, 2D Sb oxides are beginning to attract research interest in their own right^{64,77,78}. While Raman spectroscopy in Fig. 1b did not suggest significant Sb-oxide presence in our samples, close inspection of the β -Sb(001) FT in Fig. 1d reveals another, weaker intensity set of spots of sixfold symmetry at lower k-vectors (indexed “*” at ~ 0.4 nm) than the sixfold (110) β -Sb(001) spot family which is indexed in the FT. These weak inner spots may be identified with the presence of cubic Sb_2O_3 viewed along the [111] zone axis⁶⁴ (i.e., cubic $\text{Sb}_2\text{O}_3(111)$, see Supplementary Figs. 2 and 3). This poses the question whether our β -Sb deposits are partly and/or superficially oxidized during sample storage in ambient air. Some prior work has reported stability of antimonene against oxidation in the ambient conditions^{33,35,36,42,43,46,79} but other work has suggested thin antimony oxide present around Sb structures to be also prevalent^{22,23,26,38,80–82}. Notably, for the β -Sb [2-21]/cubic Sb(001) deposits no signs of additional crystalline oxides are found in (S)TEM or FT data.

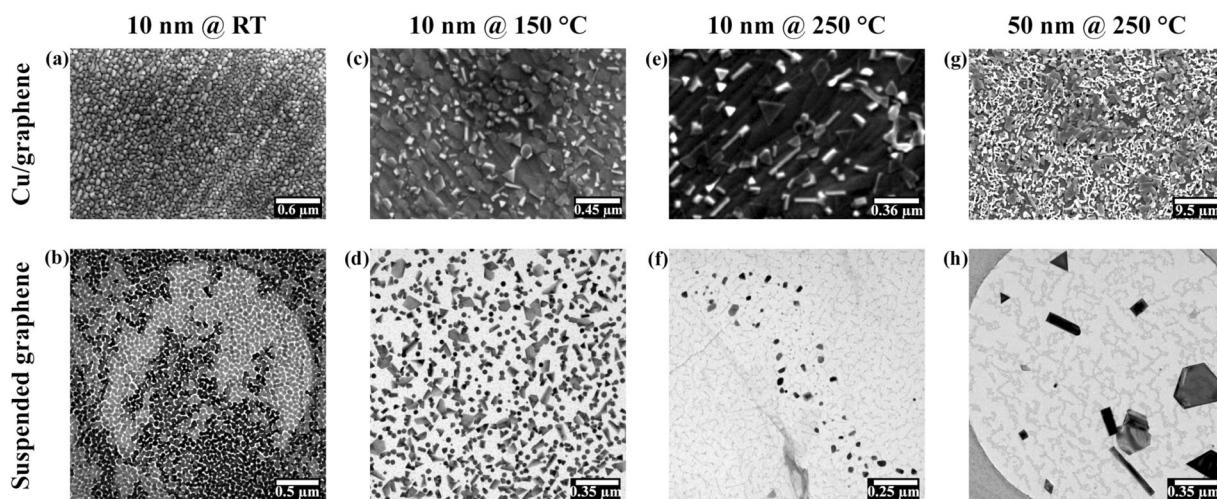


Fig. 5 Growth parameter space. Sb deposits on Cu-supported graphene (SEM in **a, c, e, g**) and suspended graphene (BF-TEM in **b, d, f, h**) deposited at nominal thicknesses of 10 nm at RT (**a, b**), 150 °C (**c, d**), and 250 °C (**e, f**) and 50 nm at 250 °C (**g, h**), respectively. **e** is replotted from Fig. 1a.

To investigate possible oxidation effects for our Sb deposits in a localized fashion, we use chemical identification via electron energy loss spectroscopy (EELS). In EELS of Sb/Sb-oxide mixtures, compositional analysis based on the commonly used EELS core loss regions is however difficult since the core loss Sb $M_{4,5}$ edge at ~ 528 eV (which follows a delayed maxima fashion) is very close/partially overlapping the O K-edge at ~ 532 eV (Supplementary Fig. 8)^{83,84}. An alternative approach is investigating the valence EELS (VEELS) low loss region in which a sharp bulk plasmon peak at ~ 16.8 eV is related to metallic Sb⁸⁵, while the plasmon peak shifts for Sb oxides to a distinctly higher energy of ~ 22 eV⁸³. For VEELS, however, also the graphene support (and, if present, amorphous carbon TEM grid membrane) has to be considered with plasmon signatures at ~ 27 eV⁸⁶.

In Fig. 4a, a typical VEELS spectrum acquired from a flat 2D β -Sb crystal (inset) is shown. We note that this particular Sb deposit was characterized by VEELS after ~ 8 months of ambient air storage, thus allowing us to probe long-term resilience against oxidation. We find that a sharp metallic Sb VEELS peak is dominating the fitted VEELS spectrum with only a small contribution of the Sb-oxide component present even after the long-term air exposure. VEELS data for β -Sb[2-21]/cubic Sb(001) deposits show similar results of only low Sb-oxide signal. The VEELS findings are thereby in agreement with the Raman data in Fig. 1b that suggested metallic Sb to be dominant in our deposits. The VEELS results however suggest the possibility of a very thin superficial oxide layer (which might be below the detection limit for Raman). This further implies for the β -Sb(001) that the inner reflections (labeled “*”) in the FT in Fig. 1d may be indeed related to a very thin crystalline cubic $Sb_2O_3(111)$ top layer on the elemental 2D β -Sb(001) crystal (where reflection “*” in Fig. 1d corresponds to the (2-20) reflection in Sb_2O_3 , see also Supplementary Figs. 2 and 3). This suggests the possibility of intrinsic Sb-oxide/Sb/graphene heterostructure formation from simple ambient air exposure. In particular, whenever present, the sixfold $Sb_2O_3(2-20)$ reflection family consistently has a rotational misorientation of $\sim 30^\circ$ with the sixfold β -Sb(110) reflection family (as in Fig. 1d). This indicates an epitaxial relation $Sb_2O_3(111)||\beta$ -Sb(001)/ $Sb_2O_3[2-20]||\beta$ -Sb[110] for the Sb-oxide/Sb interface. See Fig. 4b for an atomic model of the suggested Sb-oxide/Sb heterostructure (Sb oxide/Sb/graphene). Unfortunately, the top regions in the β -Sb flakes in our cross-section (S)TEM data are all not well enough resolved (due to Pt/C protection layers) to finally fully confirm the suggested presence of this ultrathin epitaxial Sb_2O_3 top layer. We note however that prior X-ray photoelectron spectroscopy measurements of 2D Sb

oxidation found oxide stoichiometries consistent with the here suggested crystalline Sb_2O_3 phase⁸¹, and that our core loss EELS in Supplementary Fig. 8 also is best matched with mixed Sb and Sb_2O_3 stoichiometry. No such crystalline overlayers are suggested from our data for the β -Sb[2-21]/cubic Sb(001), albeit a thin amorphous Sb-oxide overlayer is suggested to be also present based on the presence of the minor Sb-oxide signals in VEELS. Combined, our microscopic and spectroscopic data show that while our Sb deposits are overall well resilient against environmental bulk oxidation, the possibility of superficial oxidation in ambient air still requires consideration, in particular since for β -Sb(001) deposits the formation of an epitaxial $Sb_2O_3(111)$ oxide overlayer is inferred from our data.

Growth parameter space

Finally, we examine the wider parameter space of our Sb PVD. Figure 5 compares Sb deposition results of nominally 10 nm Sb (regulated via a coexposed (nonheated) QMB) as function of substrate temperature from RT to 250 °C onto CVD graphene-covered Cu foils (Fig. 5a, c, e, SEM) as well as directly onto suspended graphene membranes (no Cu underneath, Fig. 5b, d, f, TEM). Figure 5 shows that the Sb deposit morphology drastically changes between RT and elevated temperature (150 °C, 250 °C) depositions: for RT depositions (Fig. 5a, b) merged (truncated) (semi-)spherical features dominate. High-resolution STEM in Supplementary Fig. 9 shows that these RT-deposited (truncated) (semi-)spheres are amorphous. For 150 °C depositions (Fig. 5c, d) the above-described triangular/hexagonal-shaped 2D β -Sb and rod-shaped cubic Sb crystals along with few (semi-)spherical Sb deposits are found. Among the 2D β -Sb deposits the hexagonal base shape is more prevalent. For 250 °C depositions (Fig. 5e, f), practically only triangular/hexagonal-shaped 2D β -Sb and rod-shaped cubic Sb are found, whereby now among the 2D β -Sb triangles dominate. Notably, for neither 150 °C nor 250 °C we find evidence for an underlying continuous Sb layer on neither Cu-supported nor freestanding graphene, the former in contrast to the prior literature³⁸. Besides deposit morphology, also coverage and retained Sb amount of the nominally 10 nm Sb deposits is strongly influenced by substrate temperature during Sb deposition and, notably, also strongly dependent on substrate type. In particular, Sb coverage and retained Sb amount strongly decrease with increasing substrate temperature. For RT depositions, a homogeneous coverage close to 100% is achieved on both Cu-supported and freestanding graphene in Fig. 5a, b and for RT

samples good agreement between nominal 10 nm thickness and AFM-calibrated average deposit thickness was found. In comparison, the coverage for 150 and 250 °C depositions decreases, whereby the coverage decrease with substrate temperature is even more prominent on the freestanding graphene (150 °C: ~40%, 250 °C: <5%) than on the Cu-supported graphene (150 °C: ~40%, 250 °C: ~20%). For Sb deposits with an average thickness of 21 ± 14 nm at 250 °C (see above), this equates to a reduction in Sb amount deposited from RT to 250 °C of ~50% on Cu-supported graphene and of ~90% on freestanding graphene, respectively. Notably, also the size of individual deposits of Cu is significantly larger than on the suspended graphene, best seen in the 250 °C depositions (Fig. 5e, f). Combined, this suggests a key influence of temperature dependent desorption processes on Sb nanostructure growth^{35,37,47–51}. In particular, the balance of Sb adsorption flux ($F_{Sb,ad}$) from the evaporation source onto the graphene substrate and a substrate temperature-dependent Sb desorption flux from the graphene substrate into vacuum ($F_{Sb,de}(T)$) is key: the observed Sb morphologies imply that at RT $F_{Sb,ad} \gg F_{Sb,de}(RT)$ results in strong deposition, while the low temperature hinders crystallization of the resulting Sb deposits (possibly via incomplete fragmentation of physisorbed Sb_4 species which are the preferred arriving Sb vapor species⁵¹). This leads to the observed fully covering amorphous Sb deposits at RT. Increasing substrate temperature leads to a strong increase in $F_{Sb,de}(150\text{--}250\text{ °C})$, reducing the net retained amount of Sb at higher substrate temperature. In turn, the higher substrate temperatures facilitate crystallization of the retained Sb deposits (possibly via thermally activated fragmentation of surface-bound Sb species⁵¹ and thus increased Sb rearrangement). Thereby we grow crystalline Sb deposits with an onset temperature of crystallization of ~150 °C. The observation that this temperature dependence is more pronounced on freestanding graphene membranes as compared to Cu-foil supported graphene, we suggest to be related either to intrinsic substrate effects whereby the Cu surface states underneath the graphene modify, e.g., sticking coefficients to the Sb flux (akin to Cu supports modifying the surface properties of graphene in liquid wetting^{87,88}) or to a different local temperature profile on Cu-foil supported graphene vs. suspended graphene membranes due to the macroscopic thickness 25 μm Cu foils. In the latter scenario, the Cu foil acts as an effective heat sink for the additional energy arriving with the incoming Sb flux $F_{Sb,ad}$ compared to the vacuum-suspended monolayer graphene membranes (and, if present, thin amorphous carbon support), thus resulting in a (slightly) lower actual local substrate temperatures on the Cu-supported graphene.

The here observed temperature dependence of Sb deposit morphology, crystallization onset, and retained Sb amount is in good agreement with the prior literature^{35,37,47–51}. Beyond this, our results confirm that not only the directly supporting growth substrate (here, monolayer graphene) but also the supporting material underneath (here, Cu vs. vacuum) can strongly influence Sb nanostructure growth results³⁸. This is important to consider when designing Sb 2D/2D heterostructure stacks. Finally, in Fig. 5g, h, we show that the here derived understanding of the balance of adsorption, nucleation, desorption, and sub-support can also be advantageously employed to engineer larger Sb deposits of high crystalline quality. Figure 5g, h shows deposition of nominally ~50 nm Sb at 250 °C on Cu-supported (Fig. 5g) and freely suspended graphene (Fig. 5h). On the Cu-supported graphene, increasing the deposited Sb amount led not to laterally larger Sb domains but to the onset of undesired 3D Sb overgrowth (Fig. 5g). In contrast, the relatively higher desorption on the suspended graphene enabled a lower Sb nucleation density and consequently a desired larger lateral growth of remaining Sb crystallites (Fig. 5h, since presumably desorption probability decreases with increasing deposit radius). Thereby by

adjusting the substrate underneath the actual graphene support, we obtain a lateral size of >400 nm diagonal for β -Sb(001) and >500 nm long axis for β -Sb[2-21]/cubic Sb(001) deposits, respectively. This is an improvement not only over the undesired 3D Sb overgrowth from Cu/graphene supported 250 °C/50 nm but also an improvement of factor ~2 compared to the 250 °C/10 nm Cu/graphene-supported deposits. This introduces the substrate underneath the direct 2D support as an important parameter to consider in 2D Sb deposition.

In summary, using high-resolution STEM, we elucidate the structural relations in 2D Sb/graphene heterostructures which we present as a model system for 2D Sb's use in electronics and energy applications. We find two Sb morphologies to coexist under optimized deposition conditions: few-layer 2D β -Sb(001)||graphene(001) and 1D Sb which can be matched to both Sb[2-21] \perp graphene(001) and cubic Sb(001)||graphene(001). Notably, both morphologies exhibit direct in-plane rotational vdW epitaxy with the graphene support. Both morphologies are stable against ambient air oxidation even for prolonged storage, albeit superficial surface Sb-oxide formation is found. Notably, for β -Sb(001) growth of an epitaxial $Sb_2O_3(111)||\beta$ -Sb(001) overlayer is suggested from our data. While exact Sb growth results depend on growth parameters such as temperature, importantly also the nature of the support under the direct graphene support is found to have a key influence on Sb growth. Combined, our findings explore at high resolution the structural diversity in scalably fabricated 2D Sb and in 2D Sb/graphene heterostructures.

METHODS

Growth of 2D Sb and grapheme

PVD of Sb employed a commercial thermal evaporation system (MANTIS deposition system QUBE series) with a base pressure of 4×10^{-5} mbar. For PVD, Sb powder (Goodfellow, 99.999% purity, average particle size 150 μm) was loaded into a W boat, which was heated resistively to sublime the Sb. Phase diagrams⁸⁹ of W and Sb were cross-checked to ensure that no undesired intermetallics are formed during evaporation. Samples were loaded upside down over the evaporation source and behind a manual shutter. The sample table was electrically heated to a desired substrate temperature, where RT (i.e., nonheated), 150 and 250 °C were employed in this study. The Sb evaporation flux and nominally deposited thickness were monitored in situ using a nonheated QMB. The nominal Sb thickness QMB measurement was calibrated by evaporation of selected Sb films over partially masked Si wafers (thickness monitors) at RT to measure Sb film thickness over film edges by AFM. Note that the nominal thicknesses quoted in this study refer to the measured thickness values obtained from the nonheated QMB and from these Si wafer calibration depositions at RT. As discussed in the exploration of the parameter space of Sb PVD in the main text, actual retained Sb thicknesses can strongly reduce as a function of increasing substrate temperature and also type of substrate type via desorption effects.

Substrates for Sb deposition were CVD (960 °C in $CH_4/H_2/Ar$ at ~12 mbar) polycrystalline (grain size tens of μm) monolayer graphene films remaining on their 25 μm thick Cu-foil catalysts^{61,62} as well as CVD graphene films suspended as freestanding monolayer membranes over the regular hole arrays in an amorphous carbon film of a TEM grid (Quantifoil), i.e., no Cu underneath⁶³. For graphene-free reference also Cu foils without graphene were prepared as substrates by annealing at 960 °C in 12 mbar H_2 without CH_4 .

Samples were handled and stored in ambient atmosphere between ex situ graphene and 2D Sb preparation steps and STEM measurements, resulting in adventitious hydrocarbon contaminations on the graphene membranes (Figs. 1 and 5)⁵⁹, which are however typical and relevant for scalable 2D heterostructure processing⁶⁸.

Microscopic and spectroscopic measurements

The SEM employed a FEI Quanta 250 FEG SEM. TEM studies including BF imaging, SAED, (V)EELS, and energy dispersive X-ray spectroscopy (EDX, confirming the Sb purity) were performed on a FEI TECNAI F20 at 60 kV electron acceleration voltage. STEM studies were performed in an aberration-corrected Nion UltraSTEM 100 at 60 kV electron acceleration

voltage and in (high angle) ADF ((HA)ADF) mode (80–200 mrad)⁶⁰. STEM and BF-TEM image contrast was autotuned via ImageJ⁹⁰ software image by image. Correlative AFM-SEM studies employed a GETec AFSEM module installed in a FEI Quanta 600F SEM⁷¹. Conventional AFM studies employed a NT MDT NTEGRA Spectra in tapping mode⁹¹. AFM analysis employed Gwyddion software⁹². Raman spectroscopy employed a Horiba LabRAM at 532 nm laser excitation wavelength. Cross sections for TEM/STEM of Cu/graphene/Sb stacks were cut by FIB processing in a FEI Quanta 3D FEG. A protective C and Pt bilayer was deposited in FIB locally onto the region of interest prior to FIB cutting.

Phase and epitaxy analysis of Sb deposits

Phase analysis of (S)TEM data employed primarily FT/SAED pattern simulation using Highscore Plus/Pdf4+ software (ICDD Pdf4+ 2020 RDB: software version: 4.20.0.1. Database version: 4.2001.) for manual matching of measured and simulated FT/SAED patterns. In addition, also automated phase identification of measured FT/SAED data was performed using JEMS software. Structure visualization was done by Vesta⁹³ software. In particular, the following structural database entries were found to best fit our measured FT and SAED data (Pdf4+ code/Inorganic Crystal Structure Database ICSD collection code/literature reference): β -Sb: 04-14-2871/55402/ref.⁹⁴; simple cubic Sb: 04-13-3319/651499/ref.⁴⁷; and Sb₂O₃: 00-042-1466/1944/ref.⁹⁵. Notably, we checked additionally 45 other Sb and 61 other Sb-oxide entries from the ICDD Pdf4+ database which consistently gave worse matches to experimental data.

Note that β -Sb (A7, R-3m, 166) is often described in the literature not only with hexagonal axis (as here) but also with rhombohedral axis^{33,38,51}. Therefore, numerical (hkl) and [uvw] values need consideration of selected hexagonal or rhombohedral axis system, when comparing between reports. Likewise, within the hexagonal axis system some literature uses a *a*, *b* base vector inner angle of 120° (as here), while other literature uses *a*, *b* base vector inner angle of 60°^{31,33,38,51}. Again therefore comparison of numerical (hkl) and [uvw] values must consider the selected axis system. To avoid ambiguity the here used axis are typically plotted alongside the atomic models throughout the manuscript.

We calculated the average equivalent feature sizes (see main text) for the Sb deposits from their base areas (computed by ImageJ⁹⁰) in SEM and AFM data as follows: due to the different asymmetries between the characteristic base shapes for 2D triangular/hexagonal β -Sb(001) and 1D rod-like β -Sb[2-21]/cubic Sb(001), we recalculate a characteristic feature size assuming a square base shape for both phases and defining the side length of this square as the equivalent feature size.

DATA AVAILABILITY

The authors declare that the data supporting the findings of this study are available within the paper and its supplementary information files.

Received: 7 January 2021; Accepted: 1 April 2021;

Published online: 14 May 2021

REFERENCES

- Pumera, M. & Sofer, Z. 2D monoelemental arsenene, antimonene, and bismuthene: beyond black phosphorus. *Adv. Mater.* **29**, 1605299 (2017).
- Zhang, S. et al. Recent progress in 2D group-VA semiconductors: from theory to experiment. *Chem. Soc. Rev.* **47**, 982–1021 (2018).
- Ersan, F. et al. Two-dimensional pnictogens: a review of recent progresses and future research directions. *Appl. Phys. Rev.* **6**, 021308 (2019).
- Zhao, A. et al. Review of 2D group VA material-based heterostructures. *J. Phys. Appl. Phys.* **53**, 293002 (2020).
- Ares, P., Palacios, J. J., Abellán, G., Gómez-Herrero, J. & Zamora, F. Recent progress on antimonene: a new bidimensional material. *Adv. Mater.* **30**, 1703771 (2018).
- Wang, X., Song, J. & Qu, J. Antimonene: from experimental preparation to practical application. *Angew. Chem. Int. Ed.* **58**, 1574–1584 (2019).
- Zhang, S., Yan, Z., Li, Y., Chen, Z. & Zeng, H. Atomically thin arsenene and antimonene: semimetal–semiconductor and indirect–direct band-gap transitions. *Angew. Chem.* **127**, 3155–3158 (2015).
- Wang, G., Pandey, R. & Karna, S. P. Atomically thin group V elemental films: theoretical investigations of antimonene allotropes. *ACS Appl. Mater. Interfaces* **7**, 11490–11496 (2015).

- Pizzi, G. et al. Performance of arsenene and antimonene double-gate MOSFETs from first principles. *Nat. Commun.* **7**, 12585 (2016).
- Zhao, M., Zhang, X. & Li, L. Strain-driven band inversion and topological aspects in Antimonene. *Sci. Rep.* **5**, 16108 (2015).
- Qian, J. et al. High capacity Na-storage and superior cyclability of nanocomposite Sb/C anode for Na-ion batteries. *Chem. Commun.* **48**, 7070–7072 (2012).
- Zhou, X. et al. Sb nanoparticles decorated N-rich carbon nanosheets as anode materials for sodium ion batteries with superior rate capability and long cycling stability. *Chem. Commun.* **50**, 12888–12891 (2014).
- Hu, L. et al. A chemically coupled antimony/multilayer graphene hybrid as a high-performance anode for sodium-ion batteries. *Chem. Mater.* **27**, 8138–8145 (2015).
- Cheng, Y. et al. Nanostructured carbon/antimony composites as anode materials for lithium-ion batteries with long life. *Chem. Asian J.* **11**, 2173–2180 (2016).
- Liu, X. et al. Enhancing the anode performance of antimony through nitrogen-doped carbon and carbon nanotubes. *J. Phys. Chem. C* **120**, 3214–3220 (2016).
- Gu, J. et al. Liquid-phase exfoliated metallic antimony nanosheets toward high volumetric sodium storage. *Adv. Energy Mater.* **7**, 1700447 (2017).
- Cui, C. et al. Antimony nanorod encapsulated in cross-linked carbon for high-performance sodium ion battery anodes. *Nano Lett.* **19**, 538–544 (2018).
- Tian, W. et al. Few-layer antimonene: anisotropic expansion and reversible crystalline-phase evolution enable large-capacity and long-life Na-ion batteries. *ACS Nano* **12**, 1887–1893 (2018).
- Wang, H., Wu, X., Qi, X., Zhao, W. & Ju, Z. Sb nanoparticles encapsulated in 3D porous carbon as anode material for lithium-ion and potassium-ion batteries. *Mater. Res. Bull.* **103**, 32–37 (2018).
- Zhang, X. et al. Metallic Sb nanoparticles embedded in carbon nanosheets as anode material for lithium ion batteries with superior rate capability and long cycling stability. *Electrochim. Acta* **283**, 1689–1694 (2018).
- Walter, M., Erni, R. & Kovalenko, M. V. Inexpensive antimony nanocrystals and their composites with red phosphorus as high-performance anode materials for Na-ion batteries. *Sci. Rep.* **5**, 8418 (2015).
- Li, F. et al. Unlocking the electrocatalytic activity of antimony for CO₂ reduction by two-dimensional engineering of the bulk material. *Angew. Chem.* **129**, 14910–14914 (2017).
- Gusmão, R., Sofer, Z., Bouša, D. & Pumera, M. Pnictogen (As, Sb, Bi) nanosheets for electrochemical applications are produced by shear exfoliation using kitchen blenders. *Angew. Chem.* **129**, 14609–14614 (2017).
- Yu, X. et al. Emerging 2D pnictogens for catalytic applications: status and challenges. *J. Mater. Chem. A* **8**, 12887–12927 (2020).
- Martínez-Periñán, E. et al. Antimonene: a novel 2D nanomaterial for supercapacitor applications. *Adv. Energy Mater.* **8**, 1702606 (2018).
- Wang, X. et al. Bandgap-tunable preparation of smooth and large two-dimensional antimonene. *Angew. Chem.* **130**, 8804–8809 (2018).
- Chen, K.-X. et al. Excellent thermoelectric performance predicted in two-dimensional buckled antimonene: a first-principles study. *J. Phys. Chem. C* **121**, 13035–13042 (2017).
- Zhang, S. et al. Semiconducting group 15 monolayers: a broad range of band gaps and high carrier mobilities. *Angew. Chem.* **128**, 1698–1701 (2016).
- Aktürk, O. Ü., Özgelik, V. O. & Ciraci, S. Single-layer crystalline phases of antimony: antimonenes. *Phys. Rev. B* **91**, 235446 (2015).
- Hogan, C. et al. Temperature driven phase transition at the antimonene/Bi₂Se₃ van der Waals heterostructure. *ACS Nano* **13**, 10481–10489 (2019).
- Fortin-Deschênes, M. et al. Pnictogens allotropy and phase transformation during van der Waals growth. *Nano Lett.* **20**, 8258–8266 (2020).
- Lei, T. et al. Electronic structure of antimonene grown on Sb₂Te₃ (111) and Bi₂Te₃ substrates. *J. Appl. Phys.* **119**, 015302 (2016).
- Ji, J. et al. Two-dimensional antimonene single crystals grown by van der Waals epitaxy. *Nat. Commun.* **7**, 1–9 (2016).
- Tsai, H.-S., Chen, C.-W., Hsiao, C.-H., Ouyang, H. & Liang, J.-H. The advent of multilayer antimonene nanoribbons with room temperature orange light emission. *Chem. Commun.* **52**, 8409–8412 (2016).
- Fortin-Deschênes, M. et al. Synthesis of antimonene on germanium. *Nano Lett.* **17**, 4970–4975 (2017).
- Wu, X. et al. Epitaxial growth and air-stability of monolayer antimonene on PdTe₂. *Adv. Mater.* **29**, 1605407 (2017).
- Chen, H.-A. et al. Single-crystal antimonene films prepared by molecular beam epitaxy: selective growth and contact resistance reduction of the 2D material heterostructure. *ACS Appl. Mater. Interfaces* **10**, 15058–15064 (2018).
- Sun, X. et al. van der Waals epitaxy of antimony islands, sheets, and thin films on single-crystalline graphene. *ACS Nano* **12**, 6100–6108 (2018).
- Liu, X. et al. High-performance asymmetric electrodes photodiode based on Sb/WSe₂ heterostructure. *Nano Res.* **12**, 339–344 (2019).
- Shao, Y. et al. Epitaxial growth of flat antimonene monolayer: a new honeycomb analogue of graphene. *Nano Lett.* **18**, 2133–2139 (2018).

41. Mao, Y.-H. et al. Epitaxial growth of highly strained antimonene on Ag (111). *Front. Phys.* **13**, 138106 (2018).
42. Ares, P. et al. Mechanical isolation of highly stable antimonene under ambient conditions. *Adv. Mater.* **28**, 6332–6336 (2016).
43. Gibaja, C. et al. Few-layer antimonene by liquid-phase exfoliation. *Angew. Chem.* **128**, 14557–14561 (2016).
44. Fortin-Deschênes, M. et al. Dynamics of antimonene–graphene van der Waals growth. *Adv. Mater.* **31**, 1900569 (2019).
45. Märkl, T. et al. Engineering multiple topological phases in nanoscale Van der Waals heterostructures: realisation of α -antimonene. *2D Mater.* **5**, 011002 (2017).
46. Shi, Z. et al. van der Waals heteroepitaxial growth of monolayer Sb in a puckered honeycomb structure. *Adv. Mater.* **31**, 1806130 (2019).
47. Akhtar, D., Vankar, V., Goel, T. & Chopra, K. Metastable structures of liquid-quenched and vapour-quenched antimony films. *J. Mater. Sci.* **14**, 988–994 (1979).
48. Isshiki, T., Nishio, K., Saijo, H. & Shiojiri, M. Growth and crystallographic, surface and defect structures of antimony particles deposited in a high-resolution transmission electron microscope. *Thin Solid Films* **237**, 155–159 (1994).
49. Bernhardt, T. M., Stegemann, B., Kaiser, B. & Rademann, K. Crystalline structures of Sb₄ molecules in antimony thin films. *Angew. Chem. Int. Ed.* **42**, 199–202 (2003).
50. Kushvaha, S., Yan, Z., Xiao, W. & Wang, X. Surface morphology of crystalline antimony islands on graphite at room temperature. *J. Phys. Condens. Matter* **18**, 3425 (2006).
51. Yan, Z., Kushvaha, S., Xiao, W. & Wang, X.-S. Different-dimensional structures of antimony formed selectively on graphite. *Appl. Phys. A* **88**, 299–307 (2007).
52. Kolobyanina, T., Kabalkina, S., Vereshchagin, L. & Fedina, L. Investigation of the crystal structure of antimony at high pressures. *Sov. Phys. JETP* **28**, 88–90 (1969).
53. Chang, K.-J. & Cohen, M. L. Rhombohedral phase stability of the group-VA elements. *Phys. Rev. B* **33**, 7371 (1986).
54. Wang, X., Kunc, K., Loa, I., Schwarz, U. & Syassen, K. Effect of pressure on the Raman modes of antimony. *Phys. Rev. B* **74**, 134305 (2006).
55. Zouhar, M. & Šob, M. Ab initio study of deformed As, Sb, and Bi with an application to thin films. *Phys. Rev. B* **94**, 184110 (2016).
56. Sun, L. et al. Band structure and thermoelectric performances of antimony under trigonal transformation. *J. Appl. Phys.* **125**, 145102 (2019).
57. Wang, Y. & Ding, Y. The electronic structures of group-V–group-IV hetero-bilayer structures: a first-principles study. *Phys. Chem. Chem. Phys.* **17**, 27769–27776 (2015).
58. Li, W., Wang, X. & Dai, X. Tunable Schottky contacts in the antimonene/graphene van der Waals heterostructures. *Solid State Commun.* **254**, 37–41 (2017).
59. Pantelic, R. S., Meyer, J. C., Kaiser, U. & Stahlberg, H. The application of graphene as a sample support in transmission electron microscopy. *Solid State Commun.* **152**, 1375–1382 (2012).
60. Krivanek, O. L. et al. Atom-by-atom structural and chemical analysis by annular dark-field electron microscopy. *Nature* **464**, 571–574 (2010).
61. Li, X. et al. Large-area synthesis of high-quality and uniform graphene films on copper foils. *Science* **324**, 1312–1314 (2009).
62. Kidambi, P. R. et al. Observing graphene grow: catalyst–graphene interactions during scalable graphene growth on polycrystalline copper. *Nano Lett.* **13**, 4769–4778 (2013).
63. Regan, W. et al. A direct transfer of layer-area graphene. *Appl. Phys. Lett.* **96**, 113102 (2010).
64. Wu, Q. et al. Two-dimensional semiconducting and single-crystalline antimony trioxide directly-grown on monolayer graphene. *Chem. Commun.* **55**, 2473–2476 (2019).
65. Deng, Y., Handoko, A. D., Du, Y., Xi, S. & Yeo, B. S. In situ Raman spectroscopy of copper and copper oxide surfaces during electrochemical oxygen evolution reaction: identification of Cu₂O as catalytically active species. *ACS Catal.* **6**, 2473–2481 (2016).
66. Kidambi, P. R. et al. The parameter space of graphene chemical vapor deposition on polycrystalline Cu. *J. Phys. Chem. C* **116**, 22492–22501 (2012).
67. Bayer, B. C. et al. Atomic-scale in situ observations of crystallization and restructuring processes in two-dimensional MoS₂ films. *ACS Nano* **12**, 8758–8769 (2018).
68. Elibol, K. et al. Process pathway controlled evolution of phase and Van-der-Waals epitaxy in In/In₂O₃ on graphene heterostructures. *Adv. Funct. Mater.* **30**, 2003300 (2020).
69. Elibol, K. et al. Single indium atoms and few-atom indium clusters anchored onto graphene via silicon heteroatoms. <https://arxiv.org/abs/2009.00063> (2020).
70. Rathore, J. & Mahapatra, S. Formation of antimonene nanoribbons by molecular beam epitaxy. *2D Mater.* **7**, 045003 (2020).
71. Hummel, S. et al. Direct visualization of local deformations in suspended few-layer graphene membranes by coupled in situ atomic force and scanning electron microscopy. *Appl. Phys. Lett.* **118**, 103104 (2021).
72. Liu, Y., Huang, Y. & Duan, X. Van der Waals integration before and beyond two-dimensional materials. *Nature* **567**, 323–333 (2019).
73. Kim, Y. et al. Remote epitaxy through graphene enables two-dimensional material-based layer transfer. *Nature* **544**, 340–343 (2017).
74. Niu, T. et al. Modulating epitaxial atomic structure of antimonene through interface design. *Adv. Mater.* **31**, 1902606 (2019).
75. Niu, T. et al. Large-scale synthesis of strain-tunable semiconducting antimonene on copper oxide. *Adv. Mater.* **32**, 1906873 (2020).
76. Ohring, M. *Materials Science of Thin Films* (Elsevier, 2001).
77. Zhang, S. et al. Antimonene oxides: emerging tunable direct bandgap semiconductor and novel topological insulator. *Nano Lett.* **17**, 3434–3440 (2017).
78. Wolff, S., Gillen, R., Assebban, M., Abellán, G. & Maultzsch, J. Two-dimensional antimony oxide. *Phys. Rev. Lett.* **124**, 126101 (2020).
79. Wu, Q. & Song, Y. J. The environmental stability of large-size and single-crystalline antimony flakes grown by chemical vapor deposition on SiO₂ substrates. *Chem. Commun.* **54**, 9671–9674 (2018).
80. Fuchs, G. et al. Electron irradiation effects in amorphous antimony thin films obtained by cluster-beam deposition. *Philos. Mag. B* **63**, 715–725 (1991).
81. Assebban, M. et al. Unveiling the oxidation behavior of liquid-phase exfoliated antimony nanosheets. *2D Mater.* **7**, 025039 (2020).
82. Bat-Erdene, M. et al. Surface oxidized two-dimensional antimonene nanosheets for electrochemical ammonia synthesis under ambient conditions. *J. Mater. Chem. A* **8**, 4735–4739 (2020).
83. Sun, K., Liu, J. & Browning, N. Correlated atomic resolution microscopy and spectroscopy studies of Sn (Sb) O₂ nanophase catalysts. *J. Catal.* **205**, 266–277 (2002).
84. Bouchet, D., Roy, E., Yu-Zhang, K. & Leprince-Wang, Y. TEM and EELS studies of electrodeposited antimony nanowires. *Eur. Phys. J. Appl. Phys.* **30**, 193–199 (2005).
85. Wang, Y. W. et al. Antimony nanowires self-assembled from Sb nanoparticles. *J. Phys. Chem. B* **108**, 16723–16726 (2004).
86. Gass, M. H. et al. Free-standing graphene at atomic resolution. *Nat. Nanotechnol.* **3**, 676–681 (2008).
87. Rafiee, J. et al. Wetting transparency of graphene. *Nat. Mater.* **11**, 217–222 (2012).
88. Bayer, B. C., Aria, A. I., Eder, D., Hofmann, S. & Meyer, J. C. Resolving the nucleation stage in atomic layer deposition of hafnium oxide on graphene. <https://arxiv.org/abs/1909.00712> (2019).
89. Predel, B. Sb-W (antimony-tungsten). in Pu-Re–Zn-Zr, ‘Phase Equilibria, Crystallographic and Thermodynamic Data of Binary Alloys’ of Landolt-Börnstein - Group IV Physical Chemistry (Springer, 1998).
90. Abràmoff, M. D., Magalhães, P. J. & Ram, S. J. Image processing with ImageJ. *Biophotonics Int.* **11**, 36–42 (2004).
91. Elibol, K. et al. Visualising the strain distribution in suspended two-dimensional materials under local deformation. *Sci. Rep.* **6**, 28485 (2016).
92. Nečas, D. & Klapetek, P. Gwyddion: an open-source software for SPM data analysis. *Cent. Eur. J. Phys.* **10**, 181–188 (2012).
93. Momma, K. & Izumi, F. VESTA 3 for three-dimensional visualization of crystal, volumetric and morphology data. *J. Appl. Crystallogr.* **44**, 1272–1276 (2011).
94. Mozharivskij, Y., Pecharsky, A. O., Bud’ko, S. & Miller, G. J. A promising thermoelectric material: Zn₄Sb₃ or Zn₆-δSb₅. Its composition, structure, stability, and polymorphs. Structure and stability of Zn₁-δSb. *Chem. Mater.* **16**, 1580–1589 (2004).
95. Svensson, C. Refinement of the crystal structure of cubic antimony trioxide, Sb₂O₃. *Acta Crystallogr. B* **31**, 2016–2018 (1975).
96. Singh, D., Gupta, S. K., Sonvane, Y. & Lukačević, I. Antimonene: a monolayer material for ultraviolet optical nanodevices. *J. Mater. Chem. C* **4**, 6386–6390 (2016).

ACKNOWLEDGEMENTS

B.C.B., K.E., S.H., and C.M. acknowledge support from the Austrian Research Promotion Agency (FFG) under project 860382-VISION. The authors acknowledge use of the facilities at the University Service Centre for Transmission Electron Microscopy (USTEM), Vienna University of Technology (TU Wien), Austria, for parts of this work. The authors acknowledge the TU Wien Bibliothek for financial support through its Open Access Funding Program. The authors also thank TU Wien’s Doctoral College TU-D for partial support.

AUTHOR CONTRIBUTIONS

T.G., D.E., and B.C.B. planned the experiments. T.G. and K.E. carried out synthesis. T.G. performed all (S)TEM, SEM, EDX, VEELS, and Raman characterization with input from M.S.-P., C.M., and J.C.M. Author G.H. carried out FIB preparations. S.H. performed AFSEM measurements. T.G. analyzed all data with input from B.C.B. and K.E. Authors T.G. and B.C.B. wrote the manuscript with inputs from all authors.

COMPETING INTERESTS

At the time of performing of this study, S.H. had been affiliated with GETec Microscopy GmbH, Austria.

ADDITIONAL INFORMATION

Supplementary information The online version contains supplementary material available at <https://doi.org/10.1038/s41699-021-00230-3>.

Correspondence and requests for materials should be addressed to D.E. or B.C.B.

Reprints and permission information is available at <http://www.nature.com/reprints>

Publisher's note Springer Nature remains neutral with regard to jurisdictional claims in published maps and institutional affiliations.



Open Access This article is licensed under a Creative Commons Attribution 4.0 International License, which permits use, sharing, adaptation, distribution and reproduction in any medium or format, as long as you give appropriate credit to the original author(s) and the source, provide a link to the Creative Commons license, and indicate if changes were made. The images or other third party material in this article are included in the article's Creative Commons license, unless indicated otherwise in a credit line to the material. If material is not included in the article's Creative Commons license and your intended use is not permitted by statutory regulation or exceeds the permitted use, you will need to obtain permission directly from the copyright holder. To view a copy of this license, visit <http://creativecommons.org/licenses/by/4.0/>.

© The Author(s) 2021